A bubbly universe

Franco Occhionero,[1] Carlo Baccigalupi,[2,1] Luca Amendola,[1] and Stefano Monastra[1]
[1]*Osservatorio Astronomico di Roma, Viale del Parco Mellini, 84, 00136 Roma, Italy*
[2]*Dipartimento di Fisica e INFN, Università di Ferrara, Via del Paradiso 12, 44100 Ferrara, Italy*
(Received 3 June 1996; revised manuscript received 28 March 1997)

We propose to explain the present large scale structure of the universe in terms of a first order phase transition in a two field inflation: the seeds of structure are assumed to be the ensuing strong, non-Gaussian, bubblelike inhomogeneities generated by the tunneling field. Along with this, of course, the ordinary zero-point fluctuations of the slow rolling inflaton are also present: they are seen as Gaussian and small perturbations of the microwave background on the large angular scales. We describe a biparametric model of bubbles in the matter dominated era (MDE) in which caustics form at a redshift z_* in the surrounding shells and we assume that the caustics themselves are the loci of galaxy formation, i.e., the places where light is turned on. (Most likely z_* will then define also the epoch of reionization.) The two parameters are then determined by the bubble's two main features, present depth and z_*. The caustics will evolve into the shells of galaxies observed today around the nearly empty and spherical voids. Among the possible scenarios we focus on two that yield late or early caustic formation. In the MDE the shells born with the caustics experience a strong overcomoving growth (the larger the deeper is the central cavity): this phenomenon may turn bubbles substantially subdominant at decoupling (i.e., filling then only a small fraction of the available space) into the dominant features by the present time, as the observations require. For *compensated* voids, from the Sachs-Wolfe, adiabatic, and Doppler effects, we find that the largest present radii compatible with COBE amount to $\approx 100h^{-1}$ Mpc in either scenario. Thus, if the large scale structure were generated by bubbles, the present luminous universe could look bubbly up to scales of the order of one hundred Mpc mimicking a fractal with dimension $D \approx 2$ without conflicting with the isotropy of the microwave background, because homogeneity is restored thereabove. [S0556-2821(97)03324-9]

PACS number(s): 98.80.Cq, 98.80.Es

I. INTRODUCTION

One of the fundamental challenges of cosmology is to explain the variety of large-scale structures observed in current redshift surveys. Among these structures, the voids are the most prominent in terms of volume. Very recently, catalogs of voids have been compiled in the SSRS2 [1] and Infrared Astronomy Satellite (IRAS) [2] surveys. Moreover, the analysis of peculiar velocity fields shows that these voids can be really empty of matter [3]. Deep surveys give an indication that strongly underdense regions, separated by walls of matter, can extend to very large distances [4]. In a series of papers, we explored the possibility that these voids are in fact remnants of an inflationary phase transition, as first suggested by La [5,6]. In this paper we expand our previous work by modeling the bubble evolution in the matter dominated era (MDE).

In a two-field inflation [7,8], two fluctuation generating processes are at work at the same time: one is the small fluctuations of the slow rolling field ω, the other arises from the tunneling of the other field ψ toward the lower-energy minimum in the potential. At the end of inflation we will have then a bubblelike pattern imprinted over ψ, and a much more homogeneous background in ω. At reheating, the two fields convert their energy into a background of baryonic and dark matter. The present structure will in general be the result of the superposition of the two fluctuation fields. Since we will require that bubbles smaller than $100h^{-1}$ Mpc cover most of the volume by today, we assume that the large scale structure below a few hundreds Mpc is dominated by the bubblelike density fluctuations. Above this scale, no bubble has been nucleated and only the inflaton perturbations are present: therefore, homogeneity is restored, and the small ω field fluctuations match the large angle cosmic microwave background (CMB) observations as in cold dark matter (CDM) scenarios [9]. On the scales dominated by the bubbles, the galaxies are distributed mainly on surfaces, where a fractal dimension $D \approx 2$ naturally arises. In the space between bubbles, galaxies can also grow from the small scale fluctuations of the ω field: we will comment on this possibility at the end, ignoring it momentarily for the sake of clarity.

The plan of the paper is the following. In Sec. II we briefly recall the physics of primordial bubbles enucleation, with emphasis on the effective Lagrangian of fourth order gravity. In Sec. III we study the dynamics of bubble expansion in the MDE. In Sec. IV we evaluate the maximum size allowed for the bubbles by the CMB constraints. In Sec. V we draw our conclusions.

II. PRIMORDIAL BUBBLES

A convenient start is from previous work of ours [10] where the underlying physics is a fourth order gravity (FOG) obtained by adding a quadratic correction to the canonical Hilbert-Einstein action [11]

$$\mathcal{L}_{\rm grav} = -R + \frac{R^2}{6M^2 W(\psi)} \tag{2.1}$$

and by further introducing a nonminimal coupling of ψ to R^2 through $W(\psi)$ [12]. In the sequel $W(\psi)$ will act as a double well potential. The material Lagrangian $\mathcal{L}_{\rm mat}$ has instead its usual form with an ordinary potential $V(\psi)$ (in our case single welled) and the field equations are derived from $\mathcal{L}=\mathcal{L}_{\rm grav}+\mathcal{L}_{\rm mat}$. Although not all the features contained in Eq. (2.1) are essential for bubble physics to work and although one can certainly build an *ad hoc* potential in general relativity (GR) with the desired properties, and despite its complex origin, the FOG formalism is unexpectedly transparent and may be used as a toy model. In addition, it has the advantage of requiring only one scalar field ψ, the other ω being provided by gravity itself through the conformal transformation,

$$\tilde{g}_{\alpha\beta}=e^{2\omega}g_{\alpha\beta}. \tag{2.2}$$

A suitable choice of ω [13] casts the theory in Einstein's form: minimally coupled gravity with two scalar fields ω and ψ governed by a potential

$$U(\omega,\psi)=e^{-2\omega}\left[V(\psi)+\frac{3M^2}{32\pi}W(\psi)(e^{2\omega}-1)^2\right]. \tag{2.3}$$

If $W(\psi)=1+8\lambda\psi^2(\psi-\psi_0)^2/\psi_0^4$ has two degenerate vacua, these become two nondegenerate vacuum channels in $U(\omega,\psi)$, because the degeneracy is removed by $V(\psi)=(1/2)m^2\psi^2$: in Fig. 1(a) we show an example of the conformal potential shaped in the appropriate way. The motion is then a slow roll down the false vacuum (FV) channel, followed by quantum tunneling to the true vacuum (TV) channel and concluded by another slow roll down the latter channel to the absolute true vacuum. Both slow rolling phases can be described by a simple analytical approximation

$$\frac{4}{3}N=(e^{2\omega}-1), \tag{2.4}$$

where $N\approx 50\gg 1$ is the number of e foldings to the end of inflation.

Coleman's theory of bubble nucleation [14] can now be used to evaluate the number of bubbles nucleated per unit time dn_B/dt and the fraction of volume X contained in bubbles of comoving radius L [15]:

$$\frac{dX}{dL}=\left(\frac{L}{L_H}\right)^3\frac{dn_B}{dL}. \tag{2.5}$$

Two examples are given in Fig. 1(b). In the latter it is assumed that bubbles that reenter the horizon before matter-radiation equality (hereafter equivalence for shortness) are erased by radiation inflow [16]. This is schematically displayed by a vertical cut in dX/dL at $10h^{-1}$ Mpc, roughly the horizon size at equivalence: dotted curves indicate the complete spectra. The fraction of space occupied *at decoupling* by the surviving bubbles can now be evaluated [15],

$$X=\int_{10h^{-1}\,\rm Mpc}^{\infty}\frac{dX}{dL}dL, \tag{2.6}$$

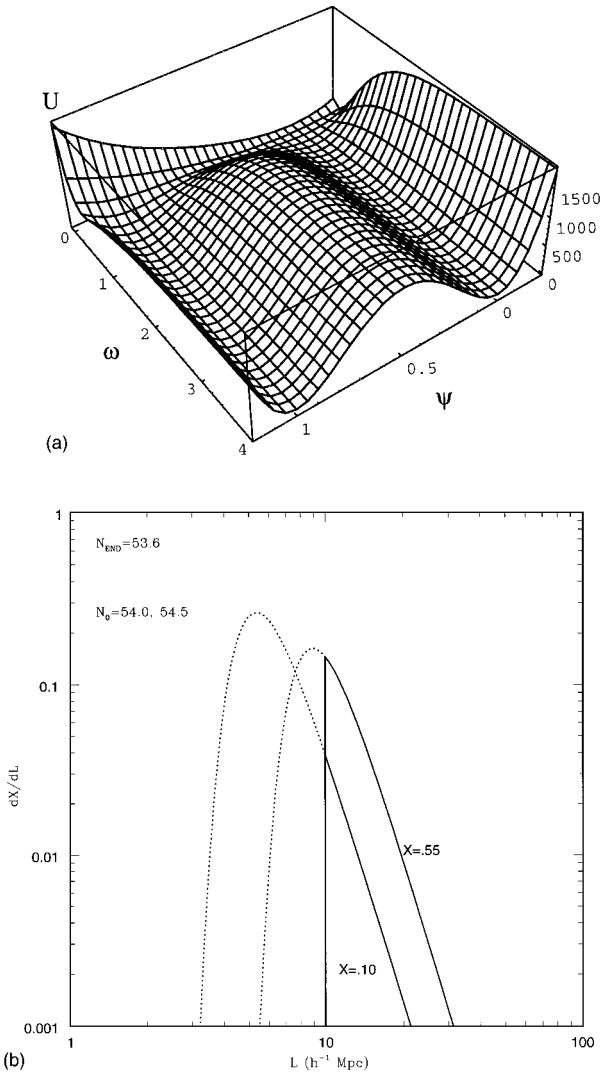

FIG. 1. (a) Potential governing the slow roll and the quantum tunneling in the special case of a two field inflation derived from a fourth order gravity. The false vacuum (FV) channel is to the left; the true vacuum (TV) channel to the right. The phase transition does not occur at the end of inflation, but some $N\approx 50$ e-foldings before. (b) Examples of bubble spectra at the end of the RDE. The assumption is that bubbles smaller than $\approx 10h^{-1}$ Mpc (approximately the horizon at equivalence) are erased by subhorizon astrophysics, hence the vertical cuts; dotted lines complete the spectra. The two spectra are obtained when a suitable parameter N_0 (approximately indicating when the phase transition is culminating) attains the values shown. A good approximation to the bubble spectra [32] is a power law $n_B(L)=(L_{\rm max}/L)^p$, where $L_{\rm max}\approx 30h^{-1}$ Mpc and $p\approx 10$.

in each case; it depends mainly on the value of N where the transition is culminating. As shown, we have in mind cases where X is definitely less than one. Correspondingly, at decoupling the $L>10h^{-1}$ Mpc bubbles do not percolate, but are embedded in a background perturbed in two ways: by the small bubbles, almost completely thermalized, and by the ordinary zero-point fluctuations, seen by the Cosmic Background Explorer (COBE) on large angular scales.

III. SPHERICAL CAUSTICS

Explosions [17,18] and underdensities [19] have long been advocated in order to generate expanding high density spherical shells, snowplowing the cosmic medium and producing galaxies in their interiors. Here we rely upon a third possibility [20], a ''metric blast'' based upon the Tolman solution—an *exact* solution of Einstein's field equations—plus a convenient energy ansatz.

Of course Newtonian physics amply suffices for such a problem (for instance (3.2) below is the simplest energy conservation): however, the use of a GR metric is necessary *i*) for the study of the null geodesics [25], and *ii*) the possible connection with the physics of bubble nucleation.

A spherical perturbation to the Hubble flow in the MDE can be described by the line element

$$ds^2=c^2dt^2-\left(\frac{\partial R}{\partial m}\right)^2\frac{dm^2}{\Gamma^2(m)}-R^2(m,t)(d\theta^2+\sin^2\theta d\phi^2), \tag{3.1}$$

where m, the observable mass, is conserved and can be used as a Lagrangian comoving coordinate. Furthermore, in the pressureless approximation $\Gamma(m)$, also a conserved quantity generalizing the Lorentz γ, is specified by the field equation

$$\Gamma^2=1+\frac{1}{c^2}\left(\frac{\partial R}{\partial t}\right)^2-\frac{2Gm}{c^2R}. \tag{3.2}$$

For a hyperbolic perturbation, i.e., an energy excess,

$$\Gamma^2(m)=1+\Gamma_+^2(m)\geqslant 1, \quad \Gamma_+(\infty)=0, \tag{3.3}$$

the solution which corresponds to an initial uniform density developing into a *compensated* cavity, takes the familiar parametric form

$$R(m,t)=\frac{Gm}{c^2\Gamma_+^2}(\cosh\eta-1),$$

$$t=\frac{Gm}{c^3\Gamma_+^3}(\sinh\eta-\eta). \tag{3.4}$$

The perturbation strength can be measured by its energy, i.e., c^2 times the difference between the gravitating mass m and the proper mass

$$m_p(m)=\int_0^m\frac{dm'}{\Gamma(m')}; \tag{3.5}$$

in the bound Newtonian case this yields the binding energy with its negative sign. Under the assumption $0<\Gamma_+^2(m)\ll 1$, it gives

$$W(\infty)=\frac{c^2}{2}\int_0^\infty dm\Gamma_+^2(m)\geqslant 0. \tag{3.6}$$

We now proceed to make an ansatz for $\Gamma_+^2(m)$ that of course guarantees the convergence of Eq. (3.6): by calling M a fiducial mass scale and after defining a dimensionless $x=m/M$, we put [20]

$$\Gamma_+^2(m)=b\times\frac{L_S}{L_D}x^{2/3}\gamma_n(x), \quad \gamma_n(0)=1,$$

$$L_S=\frac{2GM}{c^2}, \quad L_H=\frac{c}{H_0},$$

$$L=L_S^{1/3}L_H^{2/3}\approx 100h^{-2/3}\left(\frac{M}{10^{18}M_\odot}\right)^{1/3}\ \text{Mpc},$$

$$L_D=\frac{L}{(1+z_D)}, \quad \frac{L_S}{L_D}\ll 1, \tag{3.7}$$

where $1+z_D\approx 10^3$ is the redshift of the decoupling epoch. We normalize our perturbation so that Eq. (3.6) yields

$$W(\infty)=b\times\frac{3}{5}\frac{GM^2}{L_D}; \tag{3.8}$$

for this purpose in [20] we chose

$$\gamma_n(x)=\exp(-\alpha_n x^{5n/3}),$$

$$\alpha_n=\left[\frac{1}{n}\Gamma\left(\frac{1}{n}\right)\right]^n. \tag{3.9}$$

Clearly, as n grows, γ_n approximates better and better the Heaviside function; we note in passing that for $n=1$, $\alpha_1=1$ and that for $n\to\infty$ $\alpha_n\to\alpha=\exp(-\gamma_{\rm EM})=0.5614,\ldots,$ where $\gamma_{\rm EM}=0.5572,\ldots,$ is the Euler-Mascheroni constant [21].

Thus, this bubble model is characterized by (i) tunable depth, determined by b, see Eq. (3.21) below, and (ii) tunable sharpness of the outer shell, determined by n, see Eq. (3.23) below, both of which are in principle linked to the inflationary potential [34].

Density profiles can now be evaluated through the field equation

$$\rho(m,t)=\frac{1}{4\pi R^2(\partial R/\partial m)}. \tag{3.10}$$

The procedure is that $\eta(x,z)$ is first determined explicitly through the second of Eq. (3.4),

$$\sinh\eta-\eta=\frac{4}{3}B_Z^{3/2}\gamma_n^{3/2}(x), \tag{3.11}$$

where

$$B=b(1+z_D), \quad B_Z=\frac{B}{(1+z)}, \tag{3.12}$$

and then thrown into the first of Eq. (3.4) to derive the motion

$$R(m,t)=L_Z(1+z)r(x,z),$$

$$L_Z=\frac{L}{(1+z)},$$

$$r(x,z)=\frac{1}{2B}x^{1/3}\frac{\cosh\eta-1}{\gamma_n(x)}. \tag{3.13}$$

Note that the first of the above splits the physical scale L_Z from the dimensionless comoving radial distance

$$y(x,z)=(1+z)\times r(x,z); \tag{3.14}$$

also note that in front of the perturbation, in the asymptotic Hubble flow ($x\to\infty,\gamma_n\to 0$), one has $y\approx x^{1/3}$ accordingly. Instead, due to the overcomoving motion, in the perturbed region y increases with time at any fixed x.

From Eq. (3.10) we find then

$$\frac{\rho(x,z)}{\rho(\infty,z)}=\frac{x}{r^3(1+z)^3}\times\frac{1}{(3x/r)(\partial r/\partial x)}, \tag{3.15}$$

where

$$\rho(\infty,z)=\frac{3H_0^2}{8\pi G}(1+z)^3. \tag{3.16}$$

We plot with solid lines in Figs. 2–4 density profiles (3.15) vs comoving radius y, Eq. (3.14).

We now elucidate the role of the two free parameters B or b and n: a useful insight is gained from an analytic approximation for the density profiles possible for small B_Z. If we define

$$B_{\rm eff}(x,z)=B_Z\gamma_n(x)(\leqslant B_Z\ll 1), \tag{3.17}$$

we find first from Eq. (3.11) that

$$\eta(x,z)=2B_{\rm eff}^{1/2}(1-B_{\rm eff}/15), \tag{3.18}$$

and from Eq. (3.15)

$$\frac{\rho(x,z)}{\rho(\infty,z)}=\frac{1-3B_{\rm eff}/5}{1-\alpha_n nB_{\rm eff}x^{5n/3}}, \tag{3.19}$$

where the numerator corresponds to the first factor of Eq. (3.15) and the denominator to the second. Likewise, for the Hubble parameter we find

$$\frac{H(x,z)}{H(\infty,z)}=1+\frac{1}{5}B_{\rm eff}. \tag{3.20}$$

In particular at decoupling, if $B\ll 1000$,

$$\delta_D=\frac{\delta\rho}{\rho}=\frac{\rho(0,10^3)}{\rho(\infty,10^3)}-1=-\frac{3}{5}\times b, \tag{3.21}$$

which gives a simple physical meaning to b.

In [20] we gave examples only of nonsingular density profiles: we found that the larger is B the deeper is the central cavity, the rule of thumb being that, regardless of n, $B=1$ digs a hole whose central density at present is 60% of the asymptotic density: hence, to account for the observations [3] $B\gg 1$. On the other hand, increasing n at fixed B, that is sharpening the energy profile of the perturbation, sharpens the density profile of the shell around the central cavity at all epochs and hastens the formation of a caustic. In fact, unlike [20], we concentrate here on the cases where a singularity

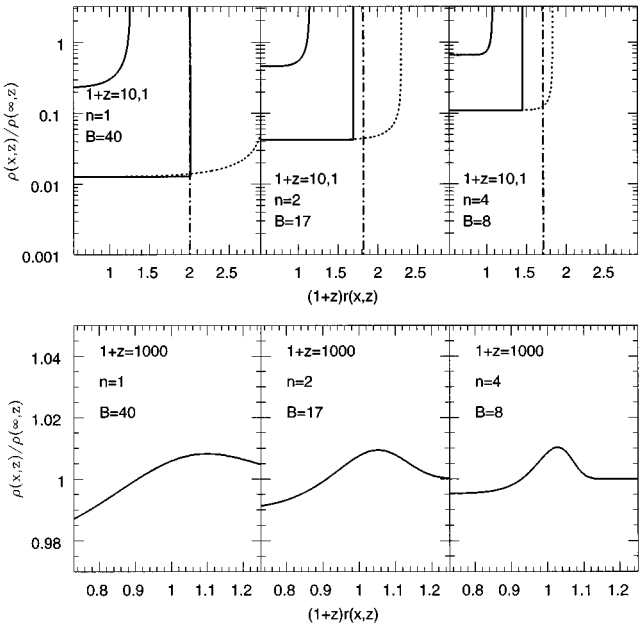

FIG. 2. Upper panel: Density profiles (solid lines) in MDE voids. The two free parameters n and B are chosen so that a caustic forms at $1+z_*=10$: for $n=1,2,4$, respectively, $B\approx 40,17,8$. Galaxies form on this caustic; furthermore the caustic sweeps up the galaxies possibly born in the interbubble space. The subsequent evolution to the present is obtained through the method of the infinitely thin shell [22]. The horizontal axis plots a comoving radial measure: it is therefore possible to read the overcomoving expansion in each case, which amounts to a factor $g\approx 2$. The volume available at the present to bubbles grows therefore by a factor of about 8. Dotted lines are derived from the Tolman solution which remains valid in the central region. Lower panel: Density profiles of the above configurations at $1+z=1000$, needed to evaluate the adiabatic and Doppler contribution. The central depth of the cavity at decoupling is given by Eq. (3.21).

$$\frac{\partial R}{\partial m}=0 \tag{3.22}$$

develops in Eq. (3.10) for the first time at a chosen redshift z_*. This implies the occurrence of shell crossing for (collisionless) DM and of shocking for (collisional) baryonic matter and signals—we assume—the first generation of galactic objects on the spherical shells and the trigger of reionization of the intergalactic gas.

In order to get a feeling of how n and B are related to z_*, we extrapolate the validity of Eq. (3.19) to the region where the denominator vanishes and we get

$$(nB)\approx e\times(1+z_*), \tag{3.23}$$

while more precise values are to be obtained from the numerical work.

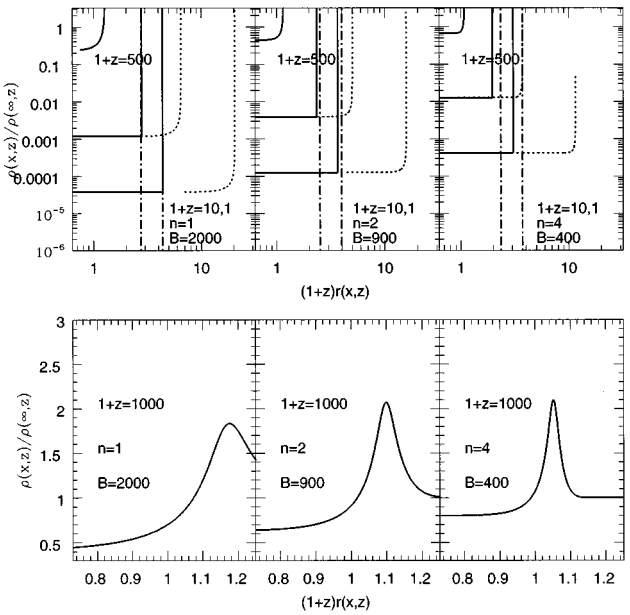

FIG. 3. Upper panel: As in Fig. 2 density profiles (solid lines) in MDE voids for early caustics: $1+z_*=500$. For $n=1,2,4$, respectively, $B\approx 2000,900,400$. Solid lines also display the position of the singular shell at $1+z=10$ and 1: the corresponding growth factors g are larger than in Fig. 2. Dashed-dotted vertical lines display the position of the singular shell obtained via Eq. (3.26): the agreement with the solid lines is very good on the left, i.e., for larger B and deeper cavities. As in Fig. 2 dotted lines are profiles derived from the Tolman solution. Lower panel: Density profiles of the above configurations at $1+z=1000$.

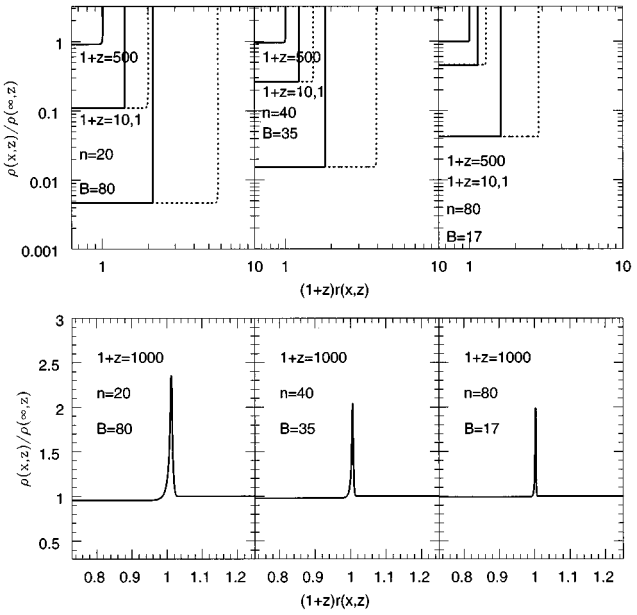

FIG. 4. Upper panel: As in Fig. 3 density profiles (solid lines) in MDE voids for early caustics: $1+z_*=500$, but now for $n=20,40,80$ and $B\approx 80,35,17$, respectively. Solid lines also display the position of the singular shell at $1+z=10$ and 1: the corresponding growth factors g are similar to those in Fig. 2. Dashed-dotted vertical lines are not given as the approximation (3.26) is now rather poor (because the initial cavity at $1+z_*=500$ is very shallow, i.e., far from the self-similar regime). Dotted lines again for the Tolman solution. Lower panel: Density profiles of the above configurations at $1+z=1000$.

After z_* the Tolman solution can yield only the extreme inner part and the extreme outer part of the density profiles, but not the intermediate part where shell crossing invalidates the dust assumption. Mathematically, this solution produces a region, bounded by two caustics, where $\partial R/\partial m<0$: an approximate expression for the x coordinates of the caustics at each z is obtained from the vanishing of the denominator of Eq. (3.19),

$$ue^{1-u}=\frac{1+z}{1+z_*},\quad u=\alpha_n x^{5n/3}. \tag{3.24}$$

For any $z<z_*$ there are in fact two such solutions, $u_{\rm inf}<1<u_{\rm sup}$, which degenerate in one, $u=1$, for $z=z_*$: for $z\ll z_*$ the corresponding two values of x also satisfy $x_{n,{\rm inf}}<1<x_{n,{\rm sup}}$, with the two roots approaching unity from below and above for $n\to\infty$, but as for y,

$$y(x_{n,{\rm inf}},z)\gg y(x_{n,{\rm sup}},z)\approx 1, \tag{3.25}$$

due to shell crossing.

Physically, however, hydrodynamics (with dissipative shocking for baryonic matter) will play a crucial role between the caustics: we will assume that a thin dense shell of galaxies (or of bound protostructures) is formed and that its position at any later time is given by the method [22] of the singular shell separating an inner Friedmann open model from an outer Friedmann flat model. In the upper panels of Figs. 2–4, solid lines give the position of the caustic at its formation, z_*, as well as the position of the singular shell at later epochs $1+z=10,1$.

The total overcomoving growth g up to the present or up to earlier times can thus be read directly from the abscissae of the vertical portion of the solid curves. Alternatively and approximately, the position of the singular shell can also be derived from the Einstein-Sedov asymptotic self-similar solution [23] $R\propto t^{4/5}$ which entails an overcomoving growth $\propto(1+z)^{-1/5}$ and is valid when the cavity is completely empty. Accordingly the total overcomoving, self-similar growth factor at any $z_{f\rm in}$ is given simply by

$$g_{ss}=y_*\times\left(\frac{1+z_*}{1+z_{f\rm in}}\right)^{1/5}, \tag{3.26}$$

where y_*, given by Eq. (3.14) at z_*, accounts for the growth already attained at z_*; g_{ss} is certainly an upper limit of g. Dotted-dashed vertical lines in the upper panels of Figs. 2 and 3 display g_{ss} at the present and at $1+z=10$. The agreement between solid and dotted-dashed lines is better the deeper the cavity and is particularly good in the left upper panels of Figs. 2 and 3 (where the central density is the lowest). Finally the density profiles derived from the Tolman solution are given by dotted lines: their inner parts are in agreement with the solid lines.

Now we can estimate by how much the fraction of space occupied by bubbles is increased by the overcomoving expansion: an $X<1$ at decoupling becomes $Y=g^3X>X$ by the present time. Whenever an $Y\gg 1$ results, an overpacking is

implied: in this case the bubbles expand overcomovingly only until they touch each other, $Y=1$, then stop their overcomoving growth and expand comovingly thereafter. For this reason, both $Y\leqslant 1$ and $Y>1$ are interesting. The second occurrence is of course more likely for larger g.

We will make use of Eq. (3.21) to classify the possible cases beginning with $n\approx 1$: (i) $B\leqslant 1$, i.e., $b\leqslant 0.001$ yields cavities shallow even at the present and must be discarded; (ii) $B\approx 1000$, i.e., $b\approx 1$ yields cavities deep at decoupling and, *a fortiori*, at the present and an early caustic formation; (iii) $1\ll B\ll 1000$, i.e., $0.001\ll b\ll 1$ yields cavities shallow at decoupling and sufficiently deep at the present and a later caustic formation. We will begin with the description of the latter intermediate case, owing to its greater simplicity.

A. Late caustics

We tipify this case by $1+z_*=10$: in order to achieve this, for $n=1,2,4$, we need, respectively, $B\approx 40,17,8$, roughly as predicted by Eq. (3.23). We display in the upper panel of Fig. 2 the density profiles of the above three cases at $1+z_*$: leftmost solid lines. These density curves as well as the next ones to be described are ideally completed by infinitely long horizontal lines of height 1 (seen only in some of the lower panels) representing the unperturbed Hubble flow ahead of the perturbation.

Physically the caustic is immediately replaced by a thin shell, the real thickness of which is to be evaluated hydrodynamically. Its exact [22] and approximate [23] positions at the present time are given by solid and by dashed-dotted lines. The agreement between the two improves the deeper the cavity. Dotted curves refer to density profiles of the Tolman solution after the caustic formation: although they are not valid in the outer region, in the inner region they agree entirely with the solid lines. Thus, for models achieving $1+z_*=10$, the total overcomoving growths are seen to amount to $g\approx 2$: this implies that, even if at decoupling the bubbles occupied only a modest 10% of the available space, they may well occupy a conspicuous 80% now. In the lower panel we display the corresponding density profiles at decoupling needed to evaluate Sachs-Wolfe, Doppler, and adiabatic effects.

B. Early caustics

We tipify this case by $1+z_*=500$, which may be achieved with large B and small n (cavities deep already at decoupling) or vice versa small B and large n (cavities still shallow at decoupling).

1. Deep cavities

With $n=1,2,4$, we need, respectively, $B\approx 2000,900,400$, again in rough agreement with Eq. (3.23). In Fig. 3, upper panels, we display with solid lines the density profiles of the above three cases at $1+z_*$ (leftmost curves) as well as the positions reached by the singular shells at the redshift $1+z=10$ and at the present time; the approximate positions evaluated via Eq. (3.26) are shown by the vertical dashed-dotted lines; dotted lines refer to the Tolman solution. In the lower panels we give the corresponding profiles at decoupling.

The maximal growths are now found to amount to $g\approx 3$ up to $1+z=10$ and to $g\approx 4$ up to the present. This case hints at a new phenomenology that may take place with these larger values of g, that $Y=g^3X$ becomes unity *before* of the present. Hence shell collisions stop the overcomoving growth and start a strictly comoving expansion: these shell collisions may themselves be a mechanism of structure formation or the origin of other interesting physics.

2. Shallow cavities

We display now some cases where $1+z_*=500$ is obtained for $n\gg 1$ and for values of B correspondingly lower than above: with $n=20,40,80$ we need, respectively, $B\approx 80,35,17$, again in rough agreement with Eq. (3.23). In Fig. 4, as before lower panels display the density profiles at decoupling: the central underdensity is smaller than in the above cases ($0.01<|\delta_D|<0.1$), but the surrounding spike is more pronounced; correspondingly shallow are the cavities at $1+z_*=500$. Upper panels display with solid lines the caustic formation and the evolution of the shell at $1+z=10,1$; dashed-dotted vertical lines derived from Eq. (3.26) are not given, because in these cases the approximation is poor (the asymptotic regime has not yet had the time to set in). These cases show overcomoving growths and density profiles comparable to those of Fig. 2.

IV. CMB CONSTRAINTS

The structures described above introduce naturally anisotropies in the CMB, particularly when placed on top of the last scattering surface (LSS). We begin by deriving the constraints for the case of an isolated bubble. We have analyzed in detail this problem in [25] and we refer there for a full treatment of the matter; in this section we report the results: the current whole-sky observations by COBE provide an upper limit of about $100h^{-1}$ Mpc to the present radius of the bubbles in both cases of early and late caustics.

A bubblelike perturbation on the LSS affects the CMB in two ways: first through the Sachs-Wolfe effect (SW) and secondly through the acoustic oscillations of the photon-baryon plasma. On the contrary, the bubbles lying in front of the LSS are generating only the Rees-Sciama effect (from the temporal change in the gravitational potential) and are neglected because their signal is very small [24,25]. We have analyzed the CMB signature of bubbles capable to generate late caustics (left panels in Fig. 5) and early ones (right panels in Fig. 5), in the sequel referred to as shallow and deep respectively with relation to the central underdensity at decoupling δ_D.

The SW effect has been evaluated by integrating null geodesics backwards in time from the observation point to the interaction with the bubble. The line-of-sight distortion naturally depends on the angle between the photon direction and the bubble center direction, on the density profile, and on the position of the bubble center with respect to the LSS. A similar approach can be found in [28]. For the width of the latter as a function of z we have taken the probability of last scattering [29]. In the upper panels of Fig. 5, we display the maximal line-of-sight distortion as a function of z for a central trajectory and for bubbles placed exactly on the LSS; the photons last scatter at $z_{\rm LSS}$ and cross the bubble toward the

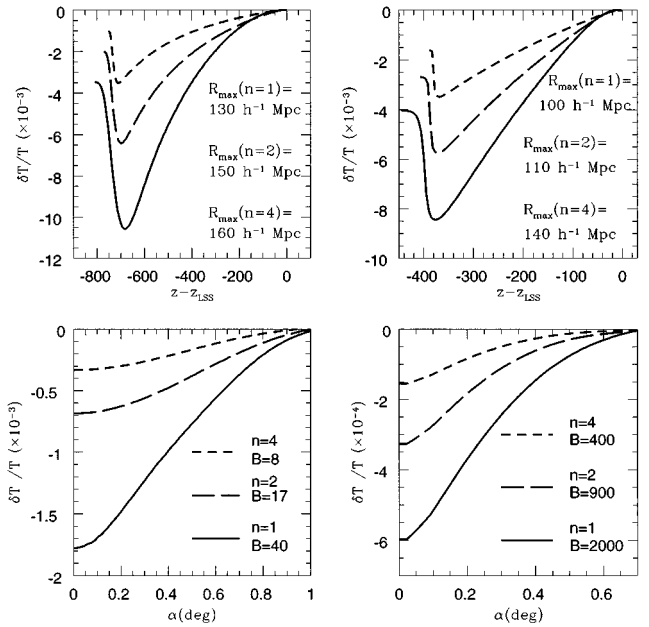

FIG. 5. Upper panels: Sachs-Wolfe effects along central trajectories for bubbles with their centers exactly on the LSS: photons traveling to the observer at $z=0$ to the left are first redshifted in the central cavity and then partially blueshifted crossing the shell. The left panel is for the late caustics (evaluated for a radius at decoupling of $75h^{-1}$ Mpc), the right panel is for the early caustics (evaluated for a radius at decoupling of $20h^{-1}$ Mpc). In each case we report the maximum radius at present allowed by COBE. Lower panels: Adiabatic and Doppler effects induced by the density perturbations of the lower panels of Figs. 2 and 3; as above, left panel for the late case, right panel for the early case.

observation to the left-hand side, where the value of the line-of-sight distortion at the observation point can be read. The larger is B (and equivalently the perturbation amplitude $|\delta_D|$), the stronger is the overall distortion; for the shallow cavities this dependence is linear. Varying the bubble's radius the signal scales as R^2 for shallow cavities, as expected for linear perturbations [26], and as R for the deep ones (precisely, in this case it is of order $R/H^{-1}/10$ [25]). For each case we display the maximal present radius $R_{\max}$ obtained by imposing that the CMB perturbation of a single bubble does not exceed the anisotropy amplitude detected by COBE. We have simulated the detection of the SW effect by mapping all the possible trajectories and modulating the signal with a Gaussian window function with $\sigma=3°$ [27]. The maximum present radius has been found to be nearly $150h^{-1}$ Mpc for shallow bubbles and $100h^{-1}$ Mpc for deep ones. Note that despite the strong difference of δ_D, the values of $R_{\max}$ are similar in the two cases; this is due to the different overcomoving growth, that compensates the more marked difference in size at decoupling; in fact the values reported of $R_{\max}$ correspond at decoupling to about $75h^{-1}$ Mpc for shallow bubbles and $25h^{-1}$ Mpc for deep ones, that are the radii chosen to perform the computations reported.

The adiabatic and Doppler effects derive from the fact that the size of our bubbles is comparable to the sound horizon at decoupling. In other words our perturbation involves scales where the pressure gradient of the photon-baryon plasma is comparable with gravitational forces. A general treatment of this situation for linear perturbations is contained in [30]: we adopted their formalism in [25] to evaluate the effect in our case. The method consists in solving the Boltzmann, Euler and continuity equations for the **k** mode of $\delta T/T$ using the Fourier transformed gravitational potential of the perturbation as a source. These equations, solved in the tight coupling approximation, account for pressure and gravitational terms, for Silk damping and for the LSS finite width. From the **k** spectrum of $\delta T/T$ we can obtain its angular profile. For this analysis, we have approximated analytically [25] the density profiles of the lower panels of Figs. 2 and 3 and we have placed the bubble on the LSS. In the lower panels of Fig. 5 we report the angular profile of $\delta T/T$ due to adiabatic and Doppler effects: the central underdensity causes a decrease of the CMB temperature, the amplitude of which increases with B as does the SW effect. The shells themselves, instead, are not seen, because Silk damping is active on their small scales. Also, Silk damping reduces the amplitude of $\delta T/T$ of deep cavities below the corresponding values for shallow ones, because of the difference in radii mentioned before. Finally, note that adiabatic and Doppler effects are generally less important than the SW one, so that it is the latter which gives the strongest CMB perturbation and which has been used to find the maximal radii $R_{\max}$.

We consider now a distribution of bubbles on the LSS: their global effect is to introduce power on the subdegree scales. Precisely, the CMB correlation function for $\delta T/T$ seen on two directions $\mathbf{n},\mathbf{n}'$ separated by an angle θ is defined as

$$\left\langle \frac{\delta T}{T}(\mathbf{n})\cdot\frac{\delta T}{T}(\mathbf{n}')\right\rangle=\sum_l \frac{2l+1}{4\pi}C_l P_l(\cos\theta), \qquad (4.1)$$

where the Legendre polynomials P_l map the amount of anisotropies (given by the C_l coefficients) at angle $\theta\simeq\pi/l$. Thus, we have that the distinctive signature on the CMB of bubbles of the maximal size derived above, is an excess power on $l\geqslant 500$ [31]: this will have to be compared with the data from the high resolution MAP and Planck missions of the near future.

V. CONCLUSIONS

Under the pressure of the new observations [1,2] we propose a new cosmogony in which large scale voids (up to hundreds of Mpc at present) originating as the primordial bubbles of a first order phase transition, are the dominant factors. By using a specific biparametric model for bubble evolution in the MDE, we have shown the compatibility of the new scenario with the CMB anisotropy known from COBE's data. On the other hand, a definite prediction for the entire CMB angular spectrum to be compared with the forthcoming high resolution experiments is being readied [31].

In the old view—that standard CDM did not have enough power to match the observations on the large scales–it was shown [32,10] that primordial bubbles/voids are capable of solving the problem, overcoming well-known [33] difficulties. Now we underline a peculiar feature of theirs, that they are also capable of generating caustics and therein galaxies at any chosen z_*, provided the parameters are adjusted suit-

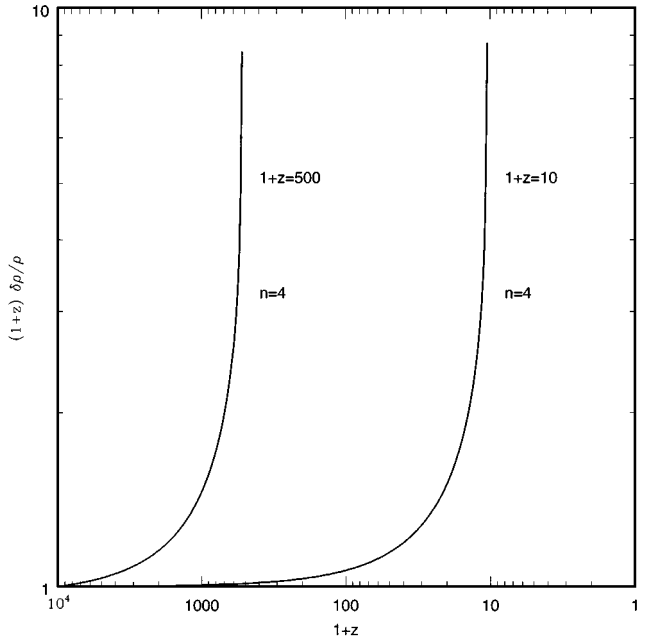

FIG. 6. Linear growth of $\delta\rho/\rho$ due to gravitational instability on the shell: what is actually plotted here is $(1+z)(\delta\rho/\rho)$, which is constant (say unity) in the surrounding background, vs $1+z$. Two of the cases described previously in Fig. 2 (late caustic, $1+z_*=10$) and in Fig. 3 (early caustic, $1+z_*=500$) are studied: in both of them, as $z\to z_*$, $\delta\rho/\rho$ diverges.

ably. In fact, as soon as the observations come up with a value for the central underdensity at the present and the theory with an indication for the epoch of reionization z_*, see, e.g., [35], then B and n can be determined in sequence as shown here. On the other hand, in our toy model [10] it is possible to relate the microphysics of bubble nucleation to astronomical observations [34] for instance about the void depth, say, at decoupling and about the bubble spectrum. It may also be underlined that, just in front of and behind the caustic, gravitational instability itself is strongly enhanced with respect to the ordinary growth law of perturbations (see the Appendix and Fig. 6).

In the light of recent debates on homogeneity vs fractality [36], it is worthwhile to point out that the present scenario is compatible with fractality, but only up to a definite scale, of the order of hundreds of Mpc, because homogeneity is restored thereabove. Perhaps not coincidentally, this scale is reminiscent of the redshift periodicities [37].

In this cosmogony, the production of galaxies occurs on the shells as described above and possibly as in conventional scenarios from the zero-point fluctuations of the inflaton in the interbubble space; the latter galaxies will gradually be swept up by the overcomoving shells and will add to the galaxies already there. The end result is a fractal distribution with $D\approx 2$. For $Y<1$ most shells will fully exploit all their available overcomoving growth without ever interacting with their neighbors. For $Y\geqslant 1$, as the observations [1,2] suggest, very commonly will a shell collide with a close neighbor; if so this will happen either late or early, in relation to whether or not the shell galaxies have had the possibility to develop fully. In either case the dominant CDM components will settle down on a plane after a few oscillations through each other: the baryonic components instead will behave differently. In the latter case the collisions between baryonic protoclouds will be higly dissipative and will often result in high angular momentum systems (protospirals?) with spin vectors oriented at random on the above plane. In the former case, the shells' protogalaxies will hardly collide with each other, but will remain anyhow trapped by the cold dark matter wall after a few oscillations through it. In either case, for galaxies this amounts to annihilating their momentum perpendicular to the wall and to letting them free to slide sideways [18]. Visually, i.e., with regard to luminous matter, the communication between the two neighboring voids opens up and the topology changes from bubbly to spongy. Finally, it is tempting to relate the observed bulk flows [38,39] to the flowing of matter on the bubble collision planes. The present scenario is therefore rich in astronomical implications which warrant further investigation.

APPENDIX: GRAVITATIONAL INSTABILITY

It is interesting to study the self-gravitating linearized growth of perturbations inside the condensing shell. The master equation

$$\left(\frac{1}{a^2}\frac{d}{dt}a^2\frac{d}{dt}-4\pi G\rho\right)\frac{\delta\rho}{\rho}=0, \tag{A1}$$

can be applied to the shell interior if a is the local scale factor $a\propto\rho^{-1/3}$. By writing now for the shell interior

$$\rho=\frac{1}{6\pi G t^2}\left(\frac{t}{t_*}\right)^{2\beta},\quad \beta>0, \tag{A2}$$

where t_* is some reference epoch, Eq. (A1) can be cast in the form

$$\left[t^2\frac{d^2}{dt^2}+\frac{4(1-\beta)}{3}t\frac{d}{dt}-\frac{2}{3}\left(\frac{t}{t_*}\right)^{2\beta}\right]\frac{\delta\rho}{\rho}=0, \tag{A3}$$

which yields the sought growing mode [21]

$$\frac{\delta\rho}{\rho}\propto t^p I_\nu\left[\sqrt{\frac{2}{3}}\frac{1}{\beta}\left(\frac{t}{t_*}\right)^{\beta}\right],$$

$$p=\frac{1}{2}+\frac{2}{3}(\beta-1),\quad \nu=\frac{p}{\beta}, \tag{A4}$$

where I_ν is the modified Bessel function of index ν.

Notice that $\beta=1$ in Eq. (A2) implies that ρ inside the shell is constant while the external density is decreasing: in fact, in that case from Eq. (A4) and [21] one recovers easily Jeans' exponential growth [see also (A5) below]; likewise $\beta>1$ implies that the density in the shell is growing: quite naturally then Eq. (A4) dictates an *overexponential* growth, i.e., that gravitational instability is formally very efficient in building structure in shrinking shells. We find in [21] the limit for large t of Eq. (A4):

$$\frac{\delta\rho}{\rho} \propto t^{(\beta-1)/6} \exp\left[\sqrt{\frac{2}{3}}\frac{1}{\beta}\left(\frac{t}{t_*}\right)^{\beta}\right]. \tag{A5}$$

Formally as β grows to ∞ during the caustic formation, the process becomes, so to speak, infinitely efficient close to the caustic itself. This can be seen directly with a numerical integration of Eq. (A1): in Fig. 6 we plot the results for the $n=4$ cases of Figs. 2 and 3. The chosen value for the comoving x is, for the sake of simplicity, $x_n=\alpha_n^{-3/5n}$, as suggested by Eq. (3.19). We plot $Z=(1+z)(\delta\rho/\rho)$ vs $(1+z)$: on approaching the caustic formation, Z, which is unity in the surrounding background, diverges.

[1] H. El-Ad, T. Piran, and L. N. Da Costa, Astrophys. J. **462**, L13 (1996).
[2] H. El-Ad, T. Piran, and L. N. Da Costa, Mon. Not. R. Astron. Soc. **287**, 790 (1997).
[3] L. N. Da Costa *et al.*, Astrophys. J. **468**, L5 (1996).
[4] J. G. Cohen, D. W. Hogg, M. A. Pahre, and R. Blandford, Astrophys. J. **462**, L9 (1996).
[5] D. La, Phys. Lett. B **265**, 232 (1991).
[6] D. La and P. J. Steinhardt, Phys. Rev. Lett. **62**, 376 (1989).
[7] F. C. Adams and K. Freese, Phys. Rev. D **43**, 353 (1991).
[8] E. W. Kolb, Phys. Scr. **T36**, 199 (1991).
[9] S. Dodelson, E. I. Gates, and M. Turner, Science **274**, 69 (1996).
[10] F. Occhionero and L. Amendola, Phys. Rev. D **50**, 4846 (1994).
[11] A. A. Starobinsky, JETP Lett. **30**, 682 (1979).
[12] L. Amendola, S. Capozziello, M. Litterio, and F. Occhionero, Phys. Rev. D **45**, 417 (1992).
[13] B. Whitt, Phys. Lett. **145B**, 176 (1984).
[14] S. Coleman, Phys. Rev. D **15**, 2929 (1977); C. Callan and S. Coleman, *ibid.* **16**, 1762 (1977); S. Coleman and F. De Luccia, *ibid.* **21**, 3305 (1980).
[15] L. Amendola, C. Baccigalupi, and F. Occhionero, Phys. Rev. D **54**, 4760 (1996).
[16] S. Vadas, Phys. Rev. D **48**, 4562 (1993).
[17] J. P. Ostriker and L. N. Cowie, Astrophys. J. Lett. **243**, L127 (1981); P. Coles and J. Barrow, Mon. Not. R. Astron. Soc. **244**, 577 (1990); R. van de Weygaert and V. Icke, Astron. Astrophys. **213**, 1 (1989).
[18] S. Yoshioka and S. Ikeuchi, Astrophys. J. **341**, 16 (1989).
[19] P. J. E. Peebles, Astrophys. J. **257**, 438 (1982); S. Shandarin and Ya. B. Zel'dovich, Rev. Mod. Phys. **61**, 185 (1989).
[20] F. Occhionero, P. Santangelo, and N. Vittorio, Astron. Astrophys. **117**, 365 (1983); F. Occhionero, L. Veccia-Scavalli, and N. Vittorio, *ibid.* **97**, 169 (1981); F. Occhionero, A. Vignato, and N. Vittorio, *ibid.* **70**, 265 (1978).
[21] M. Abramovitz and I. A. Stegun, *Handbook of Mathematical Functions* (Dover, New York, 1972).
[22] W. Israel, Nuovo Cimento B **44**, 1 (1966); V. A. Berezin, V. A. Kuzmin, and I. I. Tkachev, Phys. Rev. D **36**, 2919 (1987); N. Sakai, K. Maeda, and H. Sato, Prog. Theor. Phys. **89**, 1193 (1993).
[23] E. Bertschinger, Astrophys. J., Suppl. Ser. **58**, 1 (1985).
[24] K. L. Thompson and E. T. Vishniac, Astrophys. J. **313**, 517 (1987).
[25] C. Baccigalupi, L. Amendola, and F. Occhionero, Mon. Not. R. Astron. Soc. **288**, 387 (1997).
[26] T. Padmanabahn, *Structure Formation in the Universe* (Cambridge University Press, Cambridge, England, 1993).
[27] G. Smoot *et al.*, Astrophys. J. **396**, 489 (1992).
[28] S. L. Vadas, in *Proceedings of the Seventeenth Texas Symposium*, edited by H. Böringer *et al.* (NYAS, New York, 1995), p. 710.
[29] B. J. T. Jones and R. F. G. Wyse, Astron. Astrophys. **149**, 144 (1985).
[30] W. Hu and N. Sugiyama, Astrophys. J. **444**, 489 (1995).
[31] L. Amendola, C. Baccigalupi, and F. Occhionero, Astrophys. J. Lett. (to be published).
[32] L. Amendola and F. Occhionero, Astrophys. J. **413**, 39 (1993); L. Amendola and S. Borgani, Mon. Not. R. Astron. Soc. **266**, 191 (1994).
[33] A. R. Liddle and D. Wands, Mon. Not. R. Astron. Soc. **253**, 637 (1991).
[34] L. Amendola, C. Baccigalupi, R. Konoplich, F. Occhionero, and S. Rubin, Phys. Rev. D **54**, 7199 (1996).
[35] D. Scott, J. Silk, and M. White, Annu. Rev. Astron. Astrophys. **42**, 319 (1994).
[36] P. H. Coleman and L. Pietronero, Phys. Rep. **213**, 311 (1992); L. Pietronero and F. Sylos-Labini, in *Birth of the Universe and Fundamental Physics*, edited by F. Occhionero (Springer-Verlag, Heidelberg, 1995), p. 17; F. Sylos-Labini and L. Pietronero, *ibid.*, p. 317; F. Sylos-Labini and L. Amendola, Astrophys. J. **468**, L1 (1996); L. Pietronero, M. Montuori, and F. Sylos-Labini, in *Critical Dialogues in Cosmology*, edited by N. Turok (World Scientific, London, in press), p. 24.
[37] T. J. Broadhurst, R. S. Ellis, D. C. Koo, and A. S. Szalay, Nature (London) **343**, 726 (1990); J. Einasto *et al.*, *ibid.* **385**, 139 (1997); R. Kirshner, *ibid.* **385**, 112 (1997).
[38] T. R. Lauer and M. Postman, Astrophys. J. **400**, L47 (1992).
[39] M. A. Strauss, R. Cen, J. P. Ostriker, T. R. Lauer, and M. Postman, Astrophys. J. **444**, 507 (1996).